What Determines Meridional Heat Transport in Climate Models?

AARON DONOHOE AND DAVID S. BATTISTI

Department of Atmospheric Sciences, University of Washington, Seattle, Washington

(Manuscript received 11 May 2011, in final form 23 November 2011)

ABSTRACT

The annual mean maximum meridional heat transport (MHT_{MAX}) differs by approximately 20% among coupled climate models. The value of MHT_{MAX} can be expressed as the difference between the equator-to-pole contrast in absorbed solar radiation (ASR*) and outgoing longwave radiation (OLR*). As an example, in the Northern Hemisphere observations, the extratropics (defined as the region with a net radiative deficit) receive an 8.2-PW deficit of net solar radiation (ASR*) relative to the global average that is balanced by a 2.4-PW deficit of outgoing longwave radiation (OLR*) and 5.8 PW of energy import via the atmospheric and oceanic circulation (MHT_{MAX}). The intermodel spread of MHT_{MAX} in the Coupled Model Intercomparison Project Phase 3 (CMIP3) simulations of the preindustrial climate is primarily ($R^2 = 0.72$) due to differences in ASR* while model differences in OLR* are uncorrelated with the MHT_{MAX} spread. The net solar radiation (ASR*) is partitioned into contributions from (i) the equator-to-pole contrast in incident radiation acting on the global average albedo and (ii) the equator-to-pole contrast of planetary albedo, which is further subdivided into components due to atmospheric and surface reflection. In the observations, 62% of ASR* is due to the meridional distribution of incident radiation, 33% is due to atmospheric reflection, and 5% is due to surface reflection. The intermodel spread in ASR* is due to model differences in the equator-to-pole gradient in planetary albedo, which are primarily a consequence of atmospheric reflection differences (92% of the spread), and is uncorrelated with differences in surface reflection. As a consequence, the spread in MHT_{MAX} in climate models is primarily due to the spread in cloud reflection properties.

1. Introduction

The maximum meridional heat transport (MHT_{MAX}) in a climate system that is in equilibrium is equal to the net radiative surplus integrated over the tropics or, equivalently, the net radiative deficit integrated over the extratropics (Vonder Haar and Oort 1973). In this regard, MHT_{MAX} is equal to the equator-to-pole contrast of absorbed solar radiation (ASR) minus the equator-to-pole contrast of outgoing longwave radiation (OLR). Therefore, any change in MHT_{MAX} must be accompanied by a change in the equator-to-pole contrast of ASR or OLR without compensating changes in the other quantity. The magnitude of the MHT_{MAX} varies by approximately 20% (of order 1 PW) between the state-of-the-art coupled climate models (Lucarini and Ragone 2011). To put this number in perspective, the intermodel spread in MHT_{MAX} is approximately one order of magnitude larger than the anticipated change in MHT_{MAX} due to global warming (Held and Soden 2006). In this paper we demonstrate that the intermodel spread in MHT_{MAX} in the models used for the Intergovernmental Panel on Climate Change's (IPCC) Fourth Assessment Report (AR4) (Solomon et al. 2007) is due to intermodel differences in the equator-to-pole contrast of ASR. We then explore the processes that control the equator-to-pole contrast in ASR, its variability among climate models, and its impact on MHT_{MAX}.

In a seminal paper, Stone (1978) calculated that approximately two-thirds of the observed equator-to-pole contrast in ASR is due to the Earth–Sun geometry and the resulting meridional distribution of incident solar radiation at the top of the atmosphere (TOA) and the remaining one-third is due to the equator-to-pole contrast in planetary albedo. Stone emphasized that the latter component was nearly energetically balanced by the equator-to-pole contrast in OLR such that the equator-to-pole contrast in net radiation was equal to the ASR contrast associated with the meridional distribution of incident radiation. Subsequent work by Enderton and Marshall (2009) demonstrated that this result is not supported by modern observations or by

Corresponding author address: Aaron Donohoe, University of Washington, Box 351640, 408 ATG Bldg., Seattle, WA 98195.
E-mail: aaron@atmos.washington.edu

DOI: 10.1175/JCLI-D-11-00257.1

climate model simulations. Enderton and Marshall (2009) found that approximately 35% of the observed equator-to-pole contrast in ASR in the Northern Hemisphere and 40% in the Southern Hemisphere is due to the equator-to-pole contrast in planetary albedo and that climate states with altered meridional distributions of planetary albedo exhibit very different meridional heat transports.

Partitioning of the equator-to-pole contrast in ASR into components associated with the incident radiation (the orbital geometry) and planetary albedo is useful because, while the former is externally forced, the latter is a strong function of the climate state and thus can provide important feedbacks when the external forcing changes. More important, while the equator-to-pole contrast in incident solar radiation varies by approximately 5% over the entire obliquity cycle, there is little a priori constraint on the possible range of the equator-to-pole contrast in planetary albedo. Thus, a small perturbation in the external forcing may produce a disproportionately large change in the equator-to-pole contrast in ASR via changes in the meridional structure of planetary albedo (i.e., changes in cloud or snow/ice cover) associated with the response of the climate system. Hence, an assessment of the sources that contribute to the meridional distribution of planetary albedo is a prerequisite for understanding how and why the atmospheric and oceanic circulation (and the MHT_{MAX}) will respond to external forcing.

The earth has a pronounced equator-to-pole contrast in surface albedo due to latitudinal gradients in the fraction of area covered by ocean and land, the latitudinal gradients in land vegetation, and the spatial distribution of land and sea ice (Robock 1980). The contribution of the equator-to-pole contrast in surface albedo to the equator-to-pole contrast in planetary albedo is still an unresolved question in climate dynamics, however, because there is considerable attenuation of the surface albedo by the atmosphere. While simplified energy balance models (EBMs) have often assumed that the local planetary albedo is a function of surface albedo only (i.e., Budyko 1969; North 1975), this assumption is unwarranted due to the atmosphere's influence on planetary albedo. Indeed, the step function change of planetary albedo at the ice edge specified by EBMs is grossly inconsistent with the observed meridional structure of planetary albedo (Warren and Schneider 1979) and more recent parameterizations of planetary albedo in EBMs have suggested that the atmosphere damps the influence of surface albedo on the top-of-the-atmosphere (TOA) radiative budget (Graves et al. 1993). Recent work by Donohoe and Battisti (2011) has demonstrated that the vast majority of the global average planetary albedo is due to atmospheric as opposed to surface processes; this result suggests that the meridional gradient of planetary albedo and hence the MHT_{MAX} in the climate system may also be strongly determined by atmospheric processes (i.e., by cloud properties). For example, Trenberth and Fasullo (2010) demonstrate that model biases in the magnitude of heat transport in the Southern Hemisphere owe their existence to biases in cloud shortwave reflection in the Southern Ocean.

This paper is organized as follows. In section 2, we present the intermodel spread of MHT_{MAX} in the coupled climate models used in the IPCC's Fourth Assessment Report and how the spread in MHT_{MAX} relates to the equator-to-pole contrast of ASR and OLR. In section 3, we diagnose the processes that determine the equator-to-pole contrast in ASR in the observations and the climate models. In section 4, we examine the processes that control the intermodel spread in OLR and how these processes relate to equator-to-pole contrasts in net radiation. A discussion follows.

2. Meridional heat transport and the equator-to-pole contrast of absorbed solar radiation

In this section, we analyze the MHT_{MAX} in climate models and observations in terms of the equator-to-pole contrast of ASR and OLR. We demonstrate that the intermodel spread in peak MHT_{MAX} is largely determined by the equator-to-pole contrast of ASR.

a. Model runs and datasets used

We use data from the World Climate Research Programme's (WCRP) Coupled Model Intercomparison Project Phase 3 (CMIP3) multimodel dataset: a suite of standardized coupled simulations from 25 global climate models that were included in the International Panel on Climate Change's Fourth Assessment Report (https://esgcet.llnl.gov:8443/index.jsp). The set of model simulations is commonly referred to as the WCRP's CMIP3 multimodel dataset (Meehl et al. 2007). We use the preindustrial (PI) simulations from the 15 coupled models that provided the output fields required for the analysis presented in this study (Table 1). Each PI simulation is forced with temporally invariant external forcing (CO_2 is set to 280 ppm) and, in principle, represents an equilibrium climate that is in energy balance. In practice, both the global average and the local energy budgets are not balanced in the simulated climatologies (Lucarini and Ragone 2011). Hence, we make corrections to balance the global annual mean radiative budget by adding a spatially and temporally

TABLE 1. Models used in this study and their resolution. The horizontal resolution refers to the latitudinal and longitudinal grid spacing or the spectral truncation. The vertical resolution is the number of vertical levels.

Model	Agency, country of origin	Horizontal resolution	Vertical resolution
Bjerknes Centre for Climate Research-Bergen Climate Model version 2 (BCCR-BCM2.0)	BCCR, University of Bergen, Norway	T63	L31
Canadian Centre for Climate Modelling and Analysis (CCCma) Coupled General Circulation Model, version 3.1 (CGCM3.1)	CCCma, Canada	T47	L31
Centre National de Recherches Météorologiques Coupled Global Climate Model, version 3 (CNRM-CM3)	Météo-France/CNRM, France	T63	L45
Commonwealth Scientific and Industrial Research Organisation Mark version 3.0 (CSIRO-Mk3.0)	CSIRO, Australia	T63	L18
Geophysical Fluid Dynamics Laboratory Climate Model version 2.0 (GFDL-CM2.0)	National Oceanic and Atmospheric Administration (NOAA)/GFDL, United States	2.0° × 2.5°	L24
Goddard Institute for Space Studies Model E-R (GISS-ER)	National Aeronautics and Space Administration (NASA) GISS, United States	4° × 5°	L20
Flexible Global Ocean–Atmosphere–Land System Model gridpoint version 1.0 (FGOALS-g1.0)	Key Laboratory of Atmospheric Sciences and Geophysical Fluid Dynamics (LASG)/Institute of Atmospheric Physics (IAP), China	T42	L26
ECHAM5	Max Planck Institute for Meteorology (MPI), Germany	T63	L31
Institute of Numerical Mathematics Coupled Model, version 3.0 (INM-CM3.0)	INM, Russia	4° × 5°	L21
L'Institut Pierre-Simon Laplace Coupled Model, version 4 (IPSL-CM4)	IPSL, France	2.5° × 3.75°	L19
Model for Interdisciplinary Research on Climate 3.2, medium-resolution version [MIROC3.2(medres)]	National Institute for Environmental Studies, and Frontier Research Center for Global Change, Japan	T106	L56
Meteorological Research Institute Coupled General Circulation Model, version 2.3.2a (MRI-CGCM2.3.2a)	MRI, Japan	T42	L30
Community Climate System Model, version 3 (CCSM3)	National Center for Atmospheric Research (NCAR), United States	T85	L26
Third climate configuration of the Met Office Unified Model (UKMO-HadCM3)	Hadley Centre for Climate Prediction and Research/Met Office, United Kingdom	2.5° × 3.8°	L19
ECHAM and the global Hamburg Ocean Primitive Equation (ECHO-G)	Meteorological Institute of the University of Bonn, Germany	T30	L19

TABLE 2. Variables used in this paper.

Symbol	Meaning
MHT_{MAX}	Peak magnitude of meridional heat transport in each hemisphere
ASR*	The equator-to-pole contrast in absorbed solar radiation
OLR*	The equator-to-pole contrast of outgoing longwave radiation
x	Sine of latitude
a	Planetary coalbedo
S	Incident solar radiation
$a_{P,ATMOS}$	Atmospheric contribution to planetary albedo
$a_{P,SURF}$	Surface contribution to planetary albedo
ASR^*_{ATMOS}	Contribution of $a_{P,ATMOS}$ to ASR*
ASR^*_{SURF}	Contribution of $a_{P,SURF}$ to ASR*
LWCF	Longwave cloud forcing = $OLR–OLR_{CLEAR}$
f	Cloud fraction
C_{STRUC}	Contribution of cloud structure to OLR when clouds are present
OLR^*_{CLEAR}	Clear-sky OLR contribution to OLR*
OLR^*_{LWCF}	Contribution of LWCF to OLR*
$OLR^*_{LWCF,f}$	Contribution of cloud fraction anomalies to the intermodel spread in OLR*
$OLR^*_{LWCF,STRUC}$	Contribution of cloud structure anomalies to the intermodel spread in OLR*
TS*	Equator-to-pole contrast in surface temperature
Q^*	Equator-to-pole contrast in vertically integrated specific humidity

invariant constant to the OLR field prior to performing the analysis.[1] All calculations reported here are based on solar-weighted annual average fields.

The observational analysis makes use of the TOA and surface shortwave radiation data products from the Clouds and Earth's Radiant Energy System (CERES) experiment (Wielicki et al. 1996). We use long-term climatologies of the CERES TOA data from Fasullo and Trenberth (2008a) that are corrected for missing data and global average energy imbalances. For the surface shortwave fluxes we use the CERES "AVG" fields, which are derived by assimilating the satellite observations into a radiative transfer model to infer the surface fluxes (Rutan et al. 2001). All calculations are preformed separately for each of the four CERES instruments [Flight Models 1 and 2 (FM1 and FM2) on *Terra* from 2000 to 2005 and FM3 and FM4 on *Aqua* from 2002 to 2005]. We then average the results over the four instruments.

Observational results are provided for qualitative comparison to the models only and we caution the reader against making quanitative comparisons because (a) there are large uncertainties in the MHT_{MAX} values calculated from observations due to uncertainty in the measurements of the TOA radiative fluxes (see Wunsch 2005; Fasullo and Trenberth 2008b), (b) the observations span a short period of time, and (c) the atmospheric forcing agents between the PI simulations and the observational period differ (e.g., CO_2 and aerosols).

b. *Methodology for MHT calculation and definitions of* ASR* *and* OLR*

We determine the total (atmosphere plus ocean) zonally averaged meridional heat transport by noting that, in an equilibrium climate, the net radiative deficit spatially integrated from latitude u to the pole is exactly balanced by MHT into the region poleward of u (Trenberth and Caron 2001; Fasullo and Trenberth 2008b; Vonder Haar and Oort 1973):

$$\mathrm{MHT}(\mathsf{u}) = -2\mathsf{p}R^2 \int_{x=\sin(\mathsf{u})}^{1} [\mathrm{ASR}(x) - \mathrm{OLR}(x)]\,dx, \tag{1}$$

where x is the sine of latitude (all variables used in this paper are listed in Table 2). We gain insight into the processes that determine the maximum MHT by decomposing ASR(x) and OLR(x) into global averages (denoted by overbars) and spatial anomalies (defined as deviations from the global average and denoted by primes) and by setting the limit of integration to $x_m = \sin(\mathsf{u}_m)$, where u_m is the latitude where the zonally averaged ASR and OLR are equal. Then, Eq. (1) yields the maximum zonally averaged meridional heat transport, MHT_{MAX}:

[1] The only calculated field discussed here that is affected by this correction is the meridional heat transport; this correction ensures the global average heat transport divergence is zero and the resulting meridional heat transport is independent of whether the heat transport divergence is integrated from the South Pole to the North Pole or vice versa.

$$\mathrm{MHT}_{\mathrm{MAX}} \equiv \mathrm{MHT}(x_m) \tag{2a}$$

$$= -2\pi R^2 \times \int_{x=x_m}^{1} [\mathrm{ASR}'(x) + \overline{\mathrm{ASR}} - (\mathrm{OLR}'(x) - \overline{\mathrm{OLR}})]\, dx \tag{2b}$$

$$= -2\pi R^2 \int_{x(\mathrm{ASR}'=\mathrm{OLR}')}^{1} [\mathrm{ASR}'(x) - \mathrm{OLR}'(x)]\, dx. \tag{2c}$$

Reduction to Eq. (2c) relies on the fact that a steady climate system achieves global average radiative equilibrium:

$$\overline{\mathrm{ASR}} = \overline{\mathrm{OLR}}. \tag{3}$$

Equation (2) can be rewritten as

$$\mathrm{MHT}_{\mathrm{MAX}} \quad \mathrm{ASR}^* - \mathrm{OLR}^*, \tag{4}$$

where

$$\mathrm{ASR}^* = -2\pi R^2 \int_{x(\mathrm{ASR}'=0)}^{1} \mathrm{ASR}'\, dx \tag{5}$$

and

$$\mathrm{OLR}^* = -2\pi R^2 \int_{x(\mathrm{OLR}'=0)}^{1} \mathrm{OLR}'(x)\, dx. \tag{6}$$

The near equality in Eq. (4) holds exactly if the meridional nodes of OLR′ and ASR′ are collocated; in all calculations presented here the near equality holds to within 1% of the $\mathrm{MHT}_{\mathrm{MAX}}$ (the average error in the approximation is 0.3%). Figure 1 presents graphical representation for calculating $\mathrm{MHT}_{\mathrm{MAX}}$ from Eq. (1) (panel a) and from Eq. (4) by application of the definitions of ASR* and OLR* (panels b and c, respectively); the difference between the shaded areas in panels b and c is equal to the shaded area (representing $\mathrm{MHT}_{\mathrm{MAX}}$) in panel a.

The negative signs in Eqs. (5) and (6) are chosen so that the deficits in ASR and OLR over the extratropics render ASR* and OLR* as positive numbers. Equations (5) and (6) are the ASR and OLR deficits (ASR* and OLR*) in the Northern Hemisphere (NH) extratropics; a similar expression with modified limits of the integration holds for the Southern Hemisphere (SH). By definition, the sum of ASR* in the two hemispheres is equal to the ASR surplus (relative to the global average) integrated over the tropics. Therefore, this quantity represents the difference between the radiative energy absorbed in the

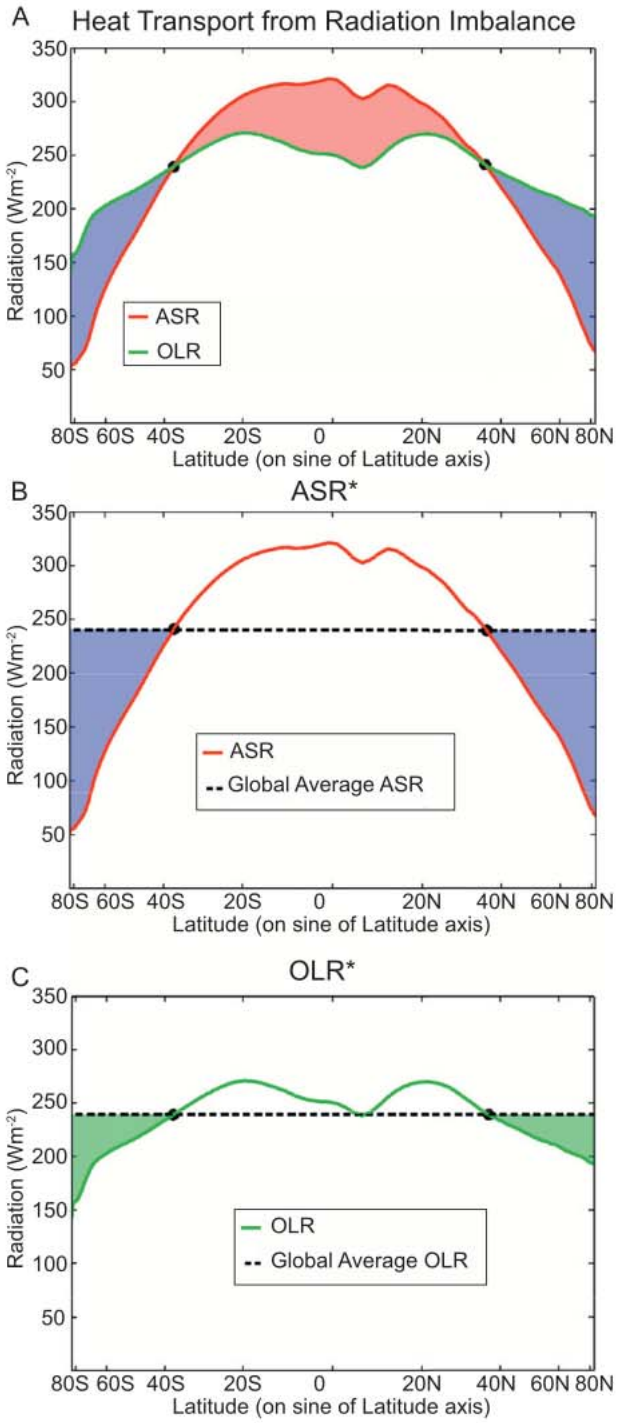

FIG. 1. Graphical demonstration of the calculations of (a) the maximum meridional heat transport ($\mathrm{MHT}_{\mathrm{MAX}}$), (b) ASR*, and (c) OLR* from the CERES annual average data. The x axis is the sine of latitude in all panels. In (a) the zonal average ASR (red line) and OLR (green line) are shown. The blue- (red-) shaded area is the spatially integrated net radiative deficit (surplus) in the extratropics (tropics) and equals the meridional heat import (export) from each region ($\mathrm{MHT}_{\mathrm{MAX}}$). In (b) the zonal average ASR is coplotted with the global average ASR; the shaded area equals ASR*. (c) Is as in (b), but for OLR and OLR*. The black dots denote the latitude where ASR′ and OLR′ = 0 in each hemisphere.

TABLE 3. Total ASR*, its partitioning into incident and net planetary albedo components (second and third columns) by application of Eq. (10) and the subsequent partitioning of the net planetary albedo component into atmospheric and surface contributions (fourth and fifth columns) by application of Eq. (12). OLR* and the MHT_{MAX} are also shown. The observations and CMIP3 multimodel average and spread (two standard deviations) are shown for each hemisphere. All entries are in PWs.

(PW)	Total ASR*	Incident	Net albedo	Atmosphere	Surface	OLR*	MHT_{MAX}
			Northern Hemisphere				
Obs	8.2	5.3	2.9	2.5	0.4	2.4	5.8
Model avg	8.1	5.2	2.9	2.4	0.5	2.6	5.5
Model spread (2s)	0.9	0.1	0.9	1.2	0.5	0.6	0.8
			Southern Hemisphere				
Obs	9.0	5.3	3.7	3.5	0.2	3.2	5.8
Model avg	8.4	5.2	3.2	2.9	0.3	3.2	5.2
Model spread (2s)	1.2	0.1	1.2	1.4	0.4	0.5	1.1

tropics and in the extratropics. In an equilibrium state, ASR* must either be balanced radiatively by OLR* or dynamically by heat transport from the tropics to the extratropics (MHT_{MAX}). In this regard, ASR* represents the equator-to-pole-scale shortwave radiation driving of the climate system and OLR* and MHT_{MAX} are the radiative and dynamic responses to the solar forcing.[2]

As a quantitative example, we calculate from the CERES data that ASR* is 8.2 PW in the NH and that this deficit in ASR over the extratropics is balanced by a 2.4-PW deficit in OLR (OLR*) and 5.8 PW of heat import via MHT_{MAX}. Similarly, in the SH extratropics, an ASR* deficit of 9.0 PW is balance by a 3.2-PW deficit in OLR* and 5.8 PW of MHT_{MAX} (Table 3).

c. Results

The CMIP3 models and the observations all have similar meridional structures of MHT (Fig. 2a) with a peak heat transport around 36° in each hemisphere. The structure and magnitude of the intermodel average MHT are in close agreement with the observational estimates of MHT in the NH[3] and MHT has a peak value (MHT_{MAX}) of 5.6 PW (Table 3). The intermodel average MHT_{MAX} in the SH is 5.3 PW, which is 0.6 PW less than observed. This result agrees with the conclusions of Trenberth and Fasullo (2010). However, the intermodel mean MHT_{MAX} in the SH is not significantly different from the observations (as assessed by a *t* test at the 95% confidence interval) given the observational error estimates of Wunsch (2005). The value of MHT_{MAX} varies widely between models (Figs. 2b,c); the intermodel spread (defined throughout as two standard deviations, 2s) in MHT_{MAX} is 0.8 PW in the NH and 1.1 PW in the SH. In the SH, the model with the largest MHT_{MAX} has approximately 50% more heat transport than the model with the smallest MHT_{MAX}.

The intermodel spread in ASR* is 0.9 PW in the NH and 1.2 PW in the SH and is approximately twice the intermodel spread in OLR* (0.5 PW in the NH and 0.6 PW in the SH). Intermodel differences in MHT_{MAX} are well correlated with the intermodel differences in ASR* (Fig. 3a) with an R^2 value of 0.57 in the NH and 0.85 in the SH (Table 4), both of which are significant at the 99% confidence interval. In contrast, MHT_{MAX} is not correlated with OLR* in either hemisphere (Fig. 3b). We can understand this result as follows. The intermodel spread in MHT_{MAX} can be diagnosed from Eq. (4) and the statistics of OLR* and ASR*:

$$\sqrt{[\langle MHT_{MAX}\rangle^2]} = \sqrt{[\langle ASR^*\rangle^2] + [\langle OLR^*\rangle^2] - 2[\langle OLR^*\rangle\langle ASR^*\rangle]}, \quad (7)$$

Where angled brackets indicate the departure of the quantity from the intermodel average and square brackets are averages over all of the models. Equation (7) demonstrates that the intermodel spread in MHT_{MAX} is a consequence of the spread in ASR*, the spread in OLR*, and the covariance between ASR* and OLR*. For example, in the limit that OLR* and ASR* are linearly independent, then the spread in MHT_{MAX} is the quadrature sum of the spread in ASR* and OLR*. In contrast, in the limit of perfect correlation between OLR* and ASR*, with a regression coefficient of unity, there would be no spread in MHT_{MAX}, independent of how much OLR* and ASR* vary between the different models. These two limits correspond to what we will call the dynamic and radiative limits of the extratropical energy budget. In the dynamic limit, departures in ASR* and OLR* from the average across the models are uncorrelated and balanced by a departure in the MHT_{MAX}. In the radiative limit, the intermodel differences in ASR*

[2] Note that ASR* is not a pure external forcing, but is itself a function of the climate system.

[3] The latter has uncertainties of approximately 20% at the latitude of peak heat transport (Wunsch 2005).

are balanced by intermodel differences in OLR* and there is no intermodel spread in MHT_{MAX}.

The square root of the intermodel covariance of OLR* and ASR* is approximately the same magnitude as the spread in OLR* and is significantly smaller than the spread in ASR* (Table 4), suggesting that the CMIP3 models are closer to the dynamic limit than the radiative limit; intermodel anomalies in ASR* and OLR* only partially balance each other leading to a MHT_{MAX} spread that is comparable in magnitude to the ASR* spread. We can understand the correlation of ASR* and MHT_{MAX} and the lack of correlation between OLR* and MHT_{MAX} from the statistics of ASR* and OLR*. Multiplying Eq. (4) by ASR*, averaging over all models, and dividing by the standard deviation of ASR* and MHT_{MAX} [from Eq. (7)] gives

$$R_{\mathrm{MHT,ASR*}} \equiv \frac{[\langle \mathrm{ASR*} \rangle \langle \mathrm{MHT_{MAX}} \rangle]}{\sqrt{[\langle \mathrm{ASR*} \rangle^2]}\sqrt{[\langle \mathrm{MHT_{MAX}} \rangle^2]}} \tag{8a}$$

$$= \frac{[\langle \mathrm{ASR*} \rangle^2] - [\langle \mathrm{ASR*} \rangle \langle \mathrm{OLR*} \rangle]}{\sqrt{[\langle \mathrm{ASR*} \rangle^2]}\sqrt{[\langle \mathrm{ASR*} \rangle^2] + [\langle \mathrm{OLR*} \rangle^2] - 2[\langle \mathrm{ASR*} \rangle \langle \mathrm{OLR*} \rangle]}}, \tag{8b}$$

where $R_{\mathrm{MHT,ASR*}}$ is the correlation coefficient between MHT_{MAX} and ASR* across the models. A similar expression holds for $R_{\mathrm{MTH,OLR*}}$. In the dynamic limit where OLR* and ASR* are uncorrelated, the fraction of the MHT_{MAX} variance explained by OLR* and ASR* is proportional to the variance of each variable and the fractional variance explained by each variable would sum to unity. In this limit 70% of the intermodel variance of MHT_{MAX} in the NH would be explained by intermodel differences in ASR* and the remaining 30% would be explained by intermodel differences in OLR*. (In the SH, 87% of the MHT_{MAX} variance would be explained by ASR* and 13% by OLR*.) For the CMIP3 simulations, however, the covariance between ASR* and OLR* reduces the variance in MHT_{MAX} explained by ASR* from 70% to 57% in the NH and from 87% to 85% in the SH. Similarly, the variance in MHT_{MAX} that is explained by OLR* is reduced from 30% in the dynamic limit to 0% in the NH and from 13% to 2% in the SH. The near-zero correlation between MHT_{MAX} and OLR* can be understood from the competing effects of the two terms in the numerator of Eq. (8b). Averaged over the ensemble members, a one-unit anomaly in OLR* is accompanied by an approximately one-unit anomaly in ASR*, because the OLR* variance is approximately equal to the covariance between ASR* and OLR* (Table 4). Thus, the typical magnitude of an ASR* anomaly associated with a given OLR* anomaly nearly balances the OLR* anomaly's impact on the extratropical energy budget leading to no correlation between OLR* and MHT_{MAX}.

In summary, the MHT_{MAX} spread in climate models is due to ASR* differences between the models because the intermodel spread in ASR* exceeds that in OLR* and because ASR* and OLR* are only weakly correlated; that is, the models are closer to the dynamic limit than the radiative limit, especially in the SH. In the remainder of this paper, we will analyze the physical processes that determine ASR*, OLR*, their intermodel spread, and their covariance.

3. The cause of differences in ASR* in the climate models

We now describe a method for partitioning ASR* into a component due to incident radiation at the TOA (Earth–Sun geometry) and a component due to the meridional gradient of planetary albedo. We then further partition the planetary albedo contribution to ASR* into a component due to atmospheric reflection and a component due to surface reflection.

a. *Partitioning of* ASR* *into incident and planetary albedo contributions*

1) METHODS

To partition ASR* into contributions due to the meridional gradient in incident solar radiation and to the meridional gradient in the planetary albedo, we write the zonal average ASR as the product of the planetary coalbedo (one minus albedo) and incident solar radiation and then expand each parameter as the sum of the global average and a spatial anomaly:

$$\begin{aligned}\mathrm{ASR}(x) &= a(x)S(x) = [\bar{a} + a'(x)][\bar{S} + S'(x)] \\ &= \underbrace{\bar{a}\bar{S}}_{\text{incident}} + \underbrace{\bar{a}S'(x)}_{\text{albedo}} + \underbrace{a'(x)\bar{S}}_{\text{net albedo}} + \underbrace{a'(x)S'(x)}_{\text{covariance}},\end{aligned} \tag{9}$$

where $a(x)$ is the coalbedo, overbars denote a spatial average, and primes indicate spatial anomalies. The

latitudinal structure of the anomaly in ASR relative to the global average ASR is given by the last three terms in Eq. (9) and is plotted in Fig. 4a. The second term on the right-hand side of Eq. (9) represents the equator-to-pole contrast in incident solar radiation multiplied by the global average coalbedo and is primarily a function of the Earth–Sun geometry; it is the equator-to-pole contrast of ASR that would exist if there were no meridional variations in planetary albedo. The third term is the contribution of inhomogeneities in planetary albedo to spatial anomalies in ASR in the absence of spatial variations of incident solar radiation (Fig. 4a). The last term is the covariance of the spatial anomalies in planetary albedo and incident radiation. The covariance contributes to a positive global average ASR because the high-latitude regions have high albedos but receive a deficit of solar radiation such that the global average planetary coalbedo ($\bar{a}$) is smaller than the global-average solar-weighted planetary coalbedo. The last term in Eq. (9) tends to have the opposite sign of (and be smaller than) the third term because in the extratropics both planetary coalbedo and insolation are lower than their global average values. Hence, the meridional gradient in ASR due to the meridional gradient in planetary albedo is overestimated by the second term alone. Therefore, we can interpret the covariance term as a correction to the planetary albedo's contribution to spatial anomalies in ASR and, for the remainder of this study, we will define the net planetary albedo contribution to ASR anomalies to be the sum of the second and third terms (Fig. 4b).[4]

By subtracting the global average of each term and integrating over the extratropics, we can calculate ASR* from Eq. (9):

$$\mathrm{ASR}^* = -2\pi R^2 \left(\bar{a} \int_{x(\mathrm{ASR}'=0)}^{1} S'(x)\,dx + \bar{S} \int_{x(\mathrm{ASR}'=0)}^{1} a'(x)\,dx + \int_{x(\mathrm{ASR}'=0)}^{1} S'(x)a'(x) - \frac{1}{2}\int_{-1}^{1} S'(x)a'(x)\,dx\,dx \right). \quad (10)$$

Equation (10) divides ASR* into an incident component due to the Earth–Sun geometry that exists in the absence of any meridional gradient in planetary albedo (the first term) and a component that owes its existence to the meridional gradient in planetary albedo (the sum of the second and third terms) that we define as the net albedo contribution to ASR*.[5]

2) RESULTS

In the observations, spatial variations in planetary albedo contribute 2.9 PW to ASR* in the NH via Eq. (10), representing 35% of the total ASR* (8.2 PW; see Table 3 and Fig. 4d). In the SH, spatial variations in planetary albedo contribute 3.7 PW to ASR* (41% of the total ASR* of 9.0 PW). The intermodel average planetary albedo contribution to ASR* in the NH is nearly identical to the observations (Table 3) whereas the models have a smaller equator-to-pole contrast in planetary albedo in the SH than is observed, resulting in smaller ASR* values (by 0.5 PW) relative to nature.

The planetary albedo contribution to ASR* varies widely between models (2σ = 0.9 PW in the NH and 1.2 PW in the SH). In contrast, the incident contribution to ASR* varies by less than 1% among the different CMIP3 models. The small intermodel spread in the incident contribution to ASR* is due to primarily to intermodel differences in global average planetary albedo and secondarily to small intermodel differences in the solar constant. The intermodel spread in the planetary albedo contribution to ASR* explains 99% of the spread in ASR* in both hemispheres. Thus, the intermodel differences in ASR* are a consequence of the intermodel differences in the meridional profile of planetary albedo.

[4] It is equally valid to interpret Eq. (9) as consisting of a component that exists in the absence of a meridional gradient in solar insolation (the second term) and a component owing its existence to the meridional gradient of solar insolation (the sum of the first and third terms). The interpretation is contingent on the phrasing of the question. In this regard, the grouping of the terms we adopt in this paper is a lower limit assessment of the planetary albedo gradient's contribution to ASR anomalies.

[5] An alternative approach to dividing the fields into a global mean and spatial anomaly is to expand the variables in terms of even Legendre polynomials in each hemisphere, as was done in Stone (1978), North (1975), and Enderton and Marshall (2009). Our ASR* and component contributions to ASR* are proportional to the second Legendre coefficients provided that the spatial structure of ASR projects entirely onto the zeroth and second Legendre polynomials. The total ASR* calculated by these two methods agrees to within 2%, the first-order terms agree to within 5% of each other, and the second-order term (the covariance) agrees to within 30%. The discrepancy is larger for the second-order term because, even if the planetary albedo and incident solar radiation were fully captured by the first two Legendre polynomials, the covariance projects primarily onto the fourth Legendre polynomial and only secondarily onto the second polynomial (i.e., note the spatial structure of the covariance term in Fig. 4b). In this regard, our index of the meridional difference is more accurate than that obtained by expansion in terms of Legendre polynomials truncated at the second-order term, although the primary conclusions reached here are independent of the methodology employed.

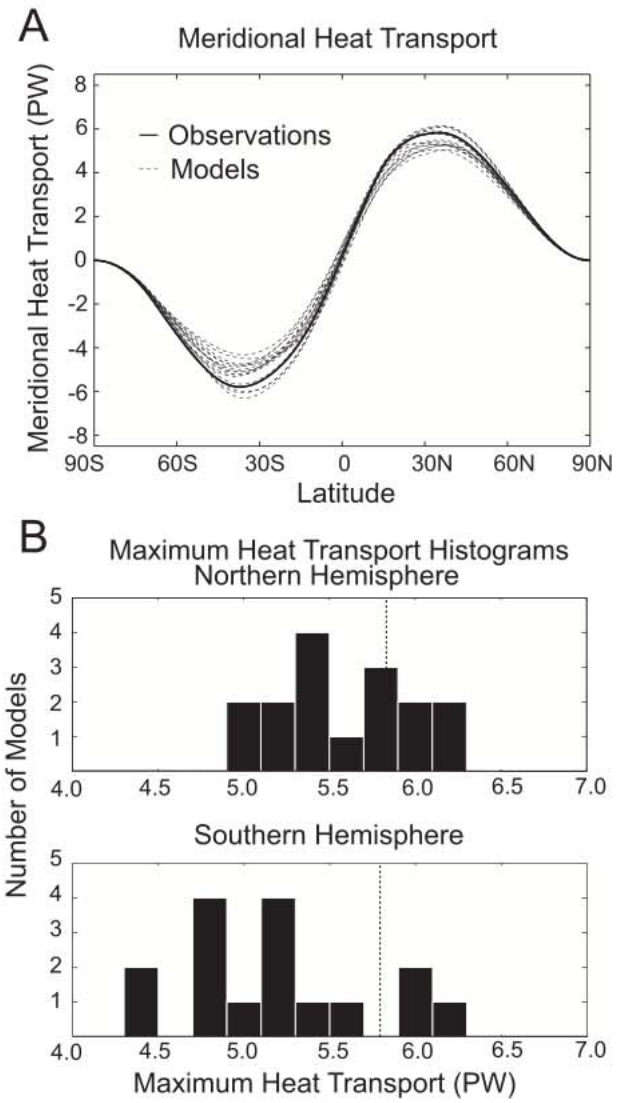

FIG. 2. (a) Meridional structure of meridional heat transport for the observations (thick-solid line) and each of the CMIP3 PI simulations (thin-dashed lines). (b) Histogram of MHT_{MAX} in the NH (top) and SH (bottom). The observed value is shown by the dashed vertical line.

b. *Partitioning of planetary albedo into atmospheric and surface components*

1) METHODOLOGY

We use the method of Donohoe and Battisti (2011) to partition the planetary albedo into a component due to reflection off of objects in the atmosphere and a component due to surface reflection. In short, their method builds a simplified radiative transfer model at each grid point that accounts for atmospheric absorption, atmospheric reflection, and surface reflection for an infinite number of passes through the atmosphere. By assuming that the atmosphere is isotropic to shortwave radiation, the simplified model provides analytical expressions for the upwelling and downwelling shortwave fluxes at both the surface and top of the atmosphere in terms of the incident radiation, the fractions of atmospheric reflection and absorption during each pass through the atmosphere, and the surface albedo. The equations can be solved for given the radiative fluxes at the TOA and the surface. The atmospheric contribution to the planetary albedo is equal to the fraction of radiation reflected during the first downward pass through the atmosphere and will be denoted as $\mathbf{a}_{P,\mathrm{ATMOS}}$. The surface contribution to planetary albedo is equal to the fraction of incident radiation that is reflected at the surface and eventually escapes into space and will be denoted as $\mathbf{a}_{P,\mathrm{SURF}}$.

We calculate $\mathbf{a}_{P,\mathrm{ATMOS}}$ and $\mathbf{a}_{P,\mathrm{SURF}}$ for both the models and observations using annual average radiative fields. We have also performed the calculations on the climatological monthly mean data from the observations and then averaged the monthly values of $\mathbf{a}_{P,\mathrm{ATMOS}}$ and $\mathbf{a}_{P,\mathrm{SURF}}$ to obtain the annual average climatology. The zonal average $\mathbf{a}_{P,\mathrm{ATMOS}}$ calculated from the monthly data agree with those calculated directly from the annual average data to within 1% of $\mathbf{a}_{P,\mathrm{ATMOS}}$ at each latitude.

2) RESULTS

In both the models and observations, the vast majority (over 85%) of the global average planetary albedo is due to $\mathbf{a}_{P,\mathrm{ATMOS}}$. The surface contribution to planetary albedo, $\mathbf{a}_{P,\mathrm{SURF}}$, is approximately one-third of the surface albedo because the atmosphere opacity attenuates the amount of incident solar radiation that reaches the surface and the amount of radiation that is reflected at the surface that escapes to space. These results are discussed at length in Donohoe and Battisti (2011). Here, we focus on the implications of these results on the intermodel spread in ASR* and MHT_{MAX}.

The contribution of $\mathbf{a}_{P,\mathrm{ATMOS}}$ and $\mathbf{a}_{P,\mathrm{SURF}}$ to spatial anomalies in ASR and ASR* can be assessed by first dividing the planetary coalbedo (a) into separate atmospheric and surface components and then writing each component in terms of a global average quantity ($\bar{}$) and the spatial departure from the global average ($'$):

$$\begin{aligned} a(x) &= 1 - \mathbf{a}_{P,\mathrm{ATMS}}(x) - \mathbf{a}_{P,\mathrm{SURF}}(x) \\ &= 1 - \bar{\mathbf{a}}_{P,\mathrm{ATMOS}} - \bar{\mathbf{a}}_{P,\mathrm{SURF}} - \mathbf{a}'_{P,\mathrm{ATMOS}}(x) \\ &\quad - \mathbf{a}'_{P,\mathrm{SURF}}(x). \end{aligned} \tag{11}$$

We then substitute the expression for $a(x)$ in Eq. (11) into Eq. (9) to define the atmospheric and surface reflection contributions to spatial anomalies in ASR (Fig. 4c). The

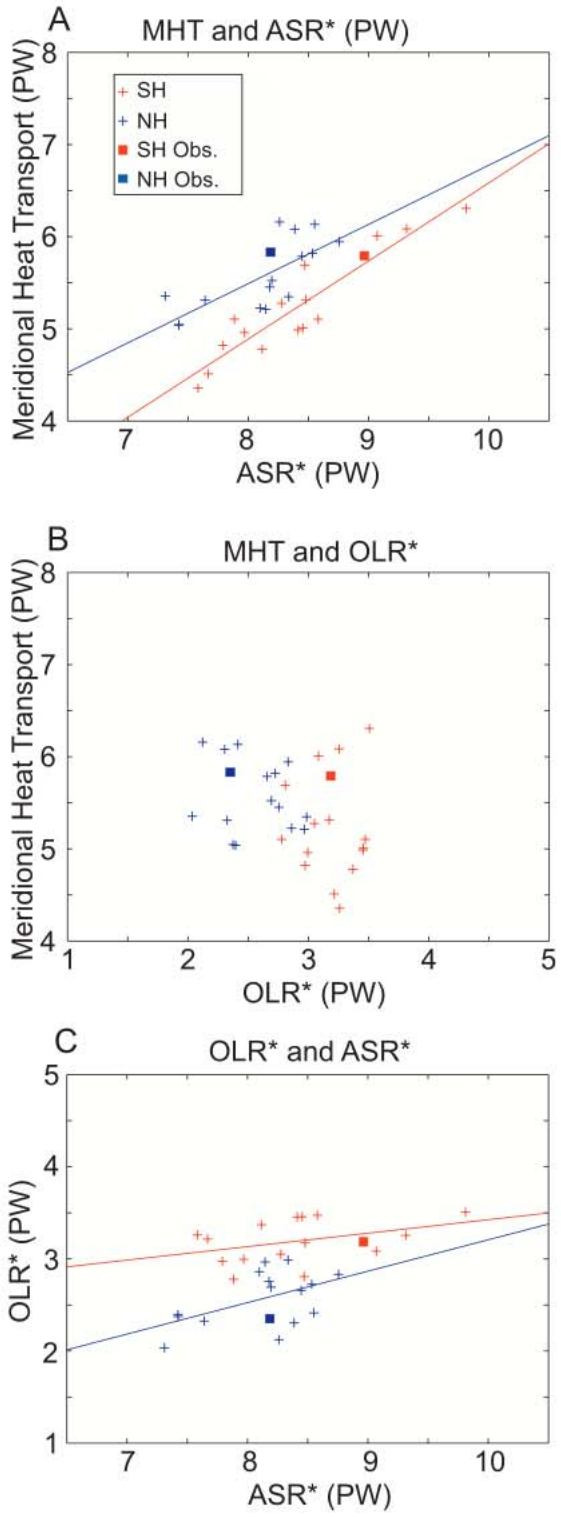

FIG. 3. (a) The MHT_{MAX} vs ASR* in the NH and SH (blue and red plus signs, respectively) of the CMIP3 PI model ensemble and observations (filled squares). (b) As in (a), but for MHT_{MAX} vs OLR*. (c) As in (a), but for OLR* vs ASR*. The blue and red lines are the linear best fits in the SH and NH and are only shown where significant.

TABLE 4. (a) The spread (2σ) in the extratropical energy budget [Eq. (4b)] in the PI simulations by the CMIP3 models. All terms are in units of PW. (b) Statistical relationships between the intermodel spread of the variables considered in this study. The squared correlation coefficients (R^2) and regression coefficients (listed in parenthesis when significant at the 99% confidence interval) are calculated separately in each hemisphere for the ensemble of 15 models listed in Table 1.

(a) Intermodel spread, 2σ (PW)

Field	NH	SH
$2\sigma_q[\overline{ASR}^q]$	0.90	1.20
$2\sigma_q[\overline{OLR}^q]$	0.58	0.46
$2\sigma_q^p[\overline{ASR}^q - \overline{OLR}^q]$	0.50	0.44
$2\sigma[\overline{MHT_{MAX}}^q]$	0.78	1.12

(b) R^2 (and regression coefficients when significant) between variables

Fields	NH	SH
MHT_{MAX} vs ASR*	0.57 (0.64)	0.85 (0.85)
MHT_{MAX} vs OLR*	0.02	0.00
OLR* vs ASR*	0.28 (0.36)	0.15 (0.15)
MHT_{MAX} vs. ASR^*_{ATMOS}	0.63	0.84
ASR* vs. ASR^*_{ATMOS}	0.80 (0.88)	0.93 (0.82)
ASR* vs. ASR^*_{SURF}	0.09	0.21(−1.32)

vast majority of the meridional gradient in ASR associated with planetary albedo inhomogeneities is due to $\alpha_{P,ATMOS}$ (Fig. 4c); $\alpha_{P,SURF}$ only contributes substantially to spatial anomalies in ASR in the region poleward of 70°, which composes a small fractional area of the extratropical domain.

Substituting Eq. (11) into Eq. (10) yields the contribution of $\alpha_{P,ATMOS}$ to ASR*, ASR^*_{ATMOS}:

$$ASR^*_{ATMOS} = 2\pi R^2 \overline{S} \int_{x(ASR'=0)}^{1} \alpha'_{P,ATMOS}\, dx + 2\pi R^2 \int_{x(ASR'=0)}^{1} \alpha'_{P,ATMOS} S' - \frac{1}{2}\int_{-1}^{1} \alpha'_{P,ATMOS} S'\, dx\, dx, \quad (12)$$

where we have again grouped the linear and covariance terms together to calculate the total contribution of the spatial structure in $\alpha_{P,ATMOS}$ to ASR* (ASR^*_{ATMOS}). A similar expression is used to calculate the contribution of $\alpha_{P,SURF}$ to ASR*, which we define as ASR^*_{SURF}. In the observations, ASR^*_{ATMOS} is found to contribute 2.5 PW to ASR* while ASR^*_{SURF} is found to contribute 0.4 PW to ASR* in the NH (Table 3). In the SH, ASR^*_{ATMOS} contributes 3.5 PW to ASR* while ASR^*_{SURF} contributes 0.2 PW to ASR*. These results suggest that, even if the equator-to-pole gradient in surface albedo were to

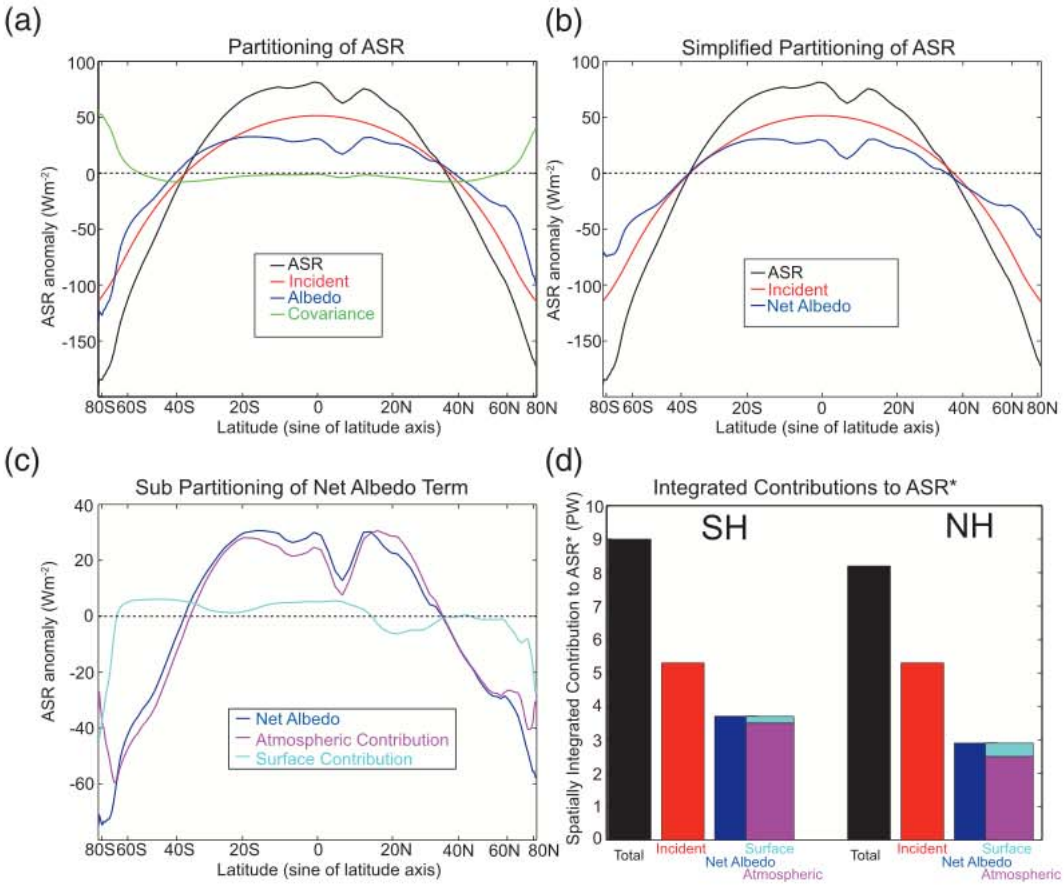

FIG. 4. (a) CERES zonal average ASR anomalies from the global average (black) partitioned into incident (red), albedo (blue), and covariance (green) terms via Eq. (10). (b) As in (a), but combining the albedo and covariance terms into a net albedo term (blue) as discussed in the text. (c) The subdivision of the net albedo term into atmospheric (magenta line) and surface reflection (cyan line) terms as discussed in section 3b. (d) The contribution of each of the terms to ASR* in each hemisphere, calculated from the spatial integral of the curves over the extratropics [colors are the same as the curves in (a)–(c)].

greatly diminish (e.g., in an ice-free world), the equator-to-pole scale gradient in ASR would decrease by less than 5% in each hemisphere, neglecting any major changes in the atmospheric reflection or absorption.

When averaged over all climate models, the breakdown of ASR* in the NH into components associated with ASR^*_{ATMOS} and ASR^*_{SURF} is similar to that in nature; the CMIP3 average ASR^*_{ATMOS} (ASR^*_{SURF}) is 2.4 PW (0.5 PW) while that observed is 2.5 PW (0.4 PW). In the SH, the CMIP3 ensemble average ASR^*_{ATMOS} is 2.9 PW, which is one model standard deviation smaller than the observed value of 3.5 PW and the ensemble average ASR^*_{SURF} is 0.3 PW, which is in close agreement with the observations (0.2 PW). These results agree with the conclusions of Trenberth and Fasullo (2010) that the model bias toward smaller than observed MHT_{MAX} in the SH (Fig. 2) is a consequence of smaller than observed equator-to-pole gradient in shortwave cloud reflection (ASR^*_{ATMOS}) due to overly transparent model clouds in the Southern Ocean. However, given an observational uncertainty in MHT_{MAX} of order 1 PW [see Wunsch (2005) for a thorough discussion] and the intermodel spread, the intermodel average MHT_{MAX} is not significantly different from the observational estimate.[6]

Figure 5 shows a scatterplot of the total ASR* against (a) ASR^*_{ATMOS} and (b) ASR^*_{SURF} from the CMIP3 models (plus signs) in the Northern (blue) and Southern (red) Hemispheres. There is a remarkably large range in the simulated ASR* (2σ = 0.9 PW and 1.2 PW in the NH and SH, respectively; see Table 3). Almost all of

[6] A propagation of errors from the observed TOA radiative fields onto ASR* and OLR* requires knowledge of the decorrelation length scale of the random and systematic errors in the CERES observations and is beyond the scope of this work.

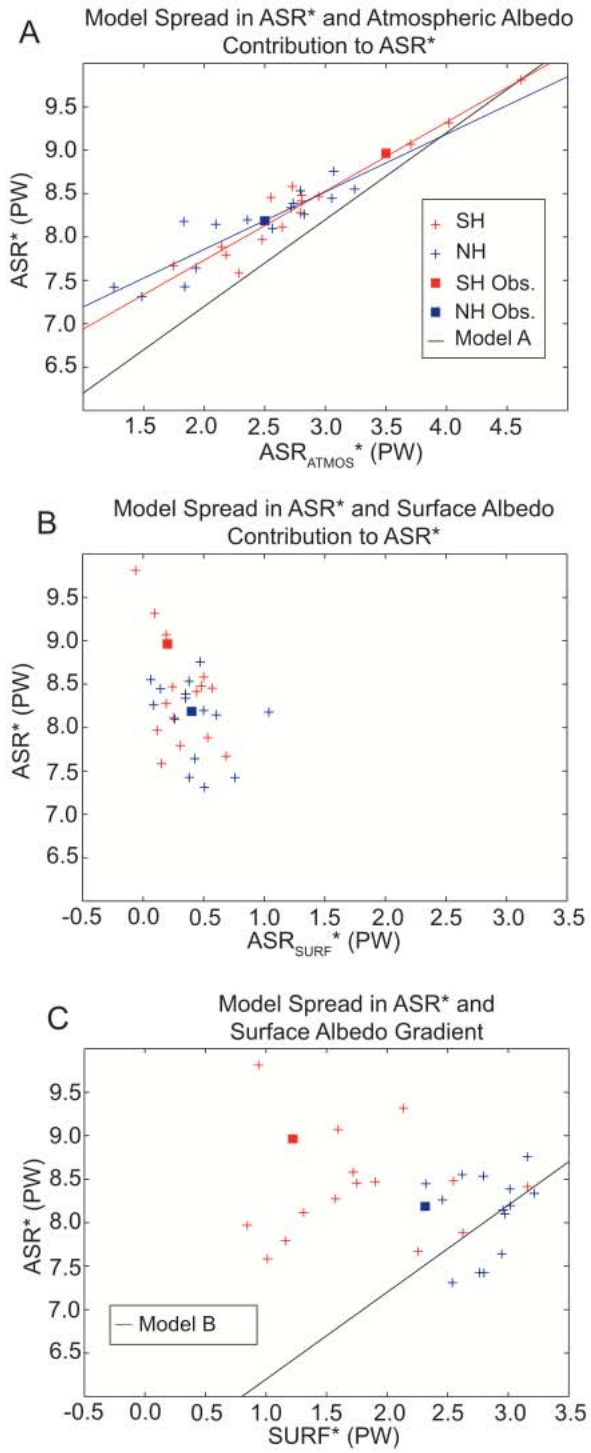

FIG. 5. (a) The ASR* vs atmospheric reflection contribution to ASR*(ASR$^*_{ATMOS}$) in the NH and SH (blue and red plus signs) of the CMIP3 PI model ensemble and observations (filled squares). The theoretical prediction of model A, as discussed in the text, is given by the black line. (b) As in (a), but plotted against the surface albedo contribution to ASR* (ASR$^*_{SURF}$). (c) As in (b), but for the surface albedo gradient (SURF*). The theoretical prediction of model B, as discussed in the text, is given by the black line. The blue and red lines are the linear best fits in the SH and NH and are only shown where significant.

the intermodel spread in ASR* is due to ASR$^*_{ATMOS}$; ASR$^*_{ATMOS}$ (2σ = 1.2 PW and 1.4 PW in the NH and SH) is highly correlated with the total ASR* (R^2 = 0.94), and the best-fit slope in each hemisphere is nearly unity. In comparison, the intermodel spread in ASR$^*_{SURF}$ is small (2σ = 0.5 PW and 0.4 PW in the NH and SH, respectively) and not correlated with total ASR*.

We take two limiting models for how the meridional structure of the atmospheric and surface reflection contribute to ASR*: model A, in which the surface albedo is spatially invariant so that ASR* is determined entirely by the spatial structure of atmospheric reflection, and model B, in which the atmosphere is transparent to shortwave radiation so that ASR* is determined entirely by the surface albedo gradient. In the case of model A, ASR* would equal the sum of the ASR$^*_{ATMOS}$ and the incident (geometric) component of 5.2 PW (Fig. 5a, black line). Model A is an excellent fit to the intermodel spread in ASR*. Model A slightly underpredicts ASR* in all cases because ASR$^*_{SURF}$ is positive in all models (the vertical offset between the black line and the individual model results in Fig. 5a). This shows that, while surface processes do play a role in determining ASR*, the majority of the intermodel spread in ASR* (94%) is explained by differences in atmospheric reflection.

At the other end of the spectrum, if the atmosphere were indeed transparent to shortwave radiation (model B), ASR* would be equal to the incident (geometric) contribution plus the surface reflection contribution given by the global average solar insolation times the surface albedo anomaly integrated over the extratropics (plus a second-order term):

$$\mathrm{SURF}^* = \overline{S}\int_{x(\mathrm{ASR}'=0)}^{1} \alpha' \, dx + \int_{x(\mathrm{ASR}'=0)}^{1} \alpha' S' - \frac{1}{2}\int_{-1}^{1} \alpha' S' \, dx \, dx, \tag{13}$$

where α' is the spatial departure of surface albedo from the global average surface albedo. In addition, SURF* is the contribution of the surface albedo to ASR* if the atmosphere were transparent to shortwave radiation (model B). The prediction of model B is coplotted with results from the CMIP3 PI simulations in Fig. 5c. Model B is clearly a poor description of the CMIP3 ensemble. Surface albedo plays a negligible role in determining the intermodel differences in ASR* because the surface albedo is strongly attenuated by the atmosphere (reflection and absorption) and the intermodel spread in atmospheric reflection overwhelms the surface albedo contribution to the planetary albedo spread.

These results demonstrate that differences in atmospheric reflection are, by far, the primary reason for the remarkable spread in ASR* in the CMIP3 ensemble of PI simulations. We previously demonstrated that the vast majority of the intermodel differences in MHT_{MAX} are due to intermodel differences in ASR* (section 2). As a consequence, intermodel differences in ASR^*_{ATMOS} explain 63% of the intermodel variance of MHT_{MAX} in the NH and 84% of the intermodel variance of MHT_{MAX} in the SH (Fig. 6). We emphasize that, although the intermodel spread in MHT_{MAX} is overwhelmingly due to differences in shortwave reflection within the atmosphere, the intermodel differences in the dynamic transports (the circulations that transport the energy) can be in either the atmosphere or the ocean (see section 5 for further discussion).

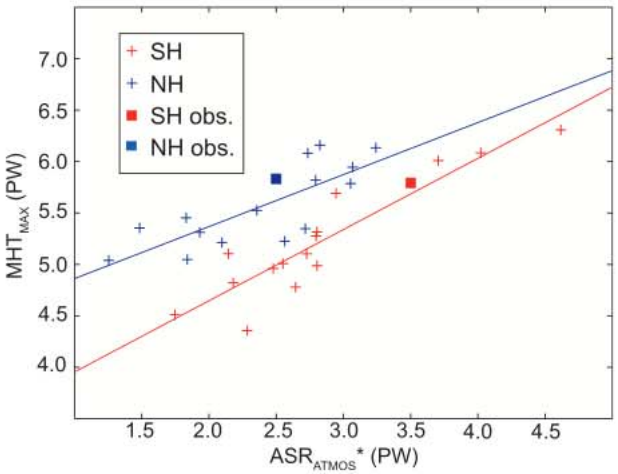

FIG. 6. The MHT_{MAX} vs atmospheric reflection contribution to ASR* (ASR^*_{ATMOS}) in the NH and SH (blue and red plus signs) of the CMIP3 PI model ensemble and observations (filled squares). The blue and red lines are the linear best fits in the SH and NH and are only shown where significant.

4. Processes controlling the intermodel spread of OLR*

In the previous sections we concluded that the CMIP3 ensemble features large differences in ASR* (due to cloud reflection differences) that are only weakly compensated by differences in OLR*, leading to large intermodel spread in MHT_{MAX}. This result is surprising because cloud longwave and shortwave radiative forcings are known to compensate for each other in the tropics (Kiehl 1994; Hartmann et al. 2001). In this section, we ask why the intermodel spreads in ASR* and OLR* do *not* compensate for each other. We first analyze the processes that cause the intermodel spread in OLR (section 4a). We then diagnose the processes that cause the intermodel spread in OLR* (section 4b) and relate the results to the intermodel spread of ASR* (section 4c).

a. *Intermodel spread in* OLR

OLR is a consequence of both clear-sky processes (i.e., temperature and specific humidity) and cloud properties (i.e., cloud optical thickness and height). We partition the intermodel spread in OLR into cloud and clear-sky contributions. We then further subpartition the cloud contribution into cloud fraction and cloud structure components and the clear-sky contribution into surface temperature and specific humidity components.

We diagnose the cloud contribution to OLR as the longwave cloud forcing (LWCF; Kiehl 1994):

$$\mathrm{LWCF} = \mathrm{OLR}_{\mathrm{CLEAR}} - \mathrm{OLR}, \qquad (14)$$

where OLR is the total-sky OLR and OLR_{CLEAR} is the clear-sky OLR. We decompose the intermodel spread in OLR into clear-sky and cloud components as follows: at each latitude, the intermodel differences in the zonal average OLR_{CLEAR} and LWCF are regressed against the intermodel differences in total OLR. The regression coefficients are then rescaled by the spread ($2\mathbf{s}$) of the total OLR at each latitude to give the clear-sky and cloud contributions to the OLR spread. By construction, the clear-sky and cloud contributions to the OLR spread add to the total-sky OLR spread (Fig. 7).

In the tropics, the intermodel spread in OLR is almost entirely due to differences in LWCF (Fig. 7a). In contrast, the intermodel spread in OLR in the polar regions is almost entirely due to differences in OLR_{CLEAR}. In the subtropics, LWCF and OLR_{CLEAR} contribute nearly equally to the OLR spread. In the SH storm-track region, LWCF contributes more to the OLR spread than OLR_{CLEAR} while the opposite is true in the NH storm-track region (presumably because, in the midlatitudes, land covers a larger fraction of the area in the NH than in the SH).

We further divide the intermodel spread in LWCF into components due intermodel differences in cloud fraction and cloud structure. The total-sky OLR can be written as the cloud fraction (f) weighted sum of the OLR when the scene is clear (OLR_{CLEAR}) and the OLR when the scene is cloudy (OLR_{CLOUD}):

$$\begin{aligned}\mathrm{OLR} &= (1-f)\mathrm{OLR}_{\mathrm{CLEAR}} + f(\mathrm{OLR}_{\mathrm{CLOUD}}) \\ &= \mathrm{OLR}_{\mathrm{CLEAR}} + f(\mathrm{OLR}_{\mathrm{CLOUD}} - \mathrm{OLR}_{\mathrm{CLEAR}}).\end{aligned} \qquad (15)$$

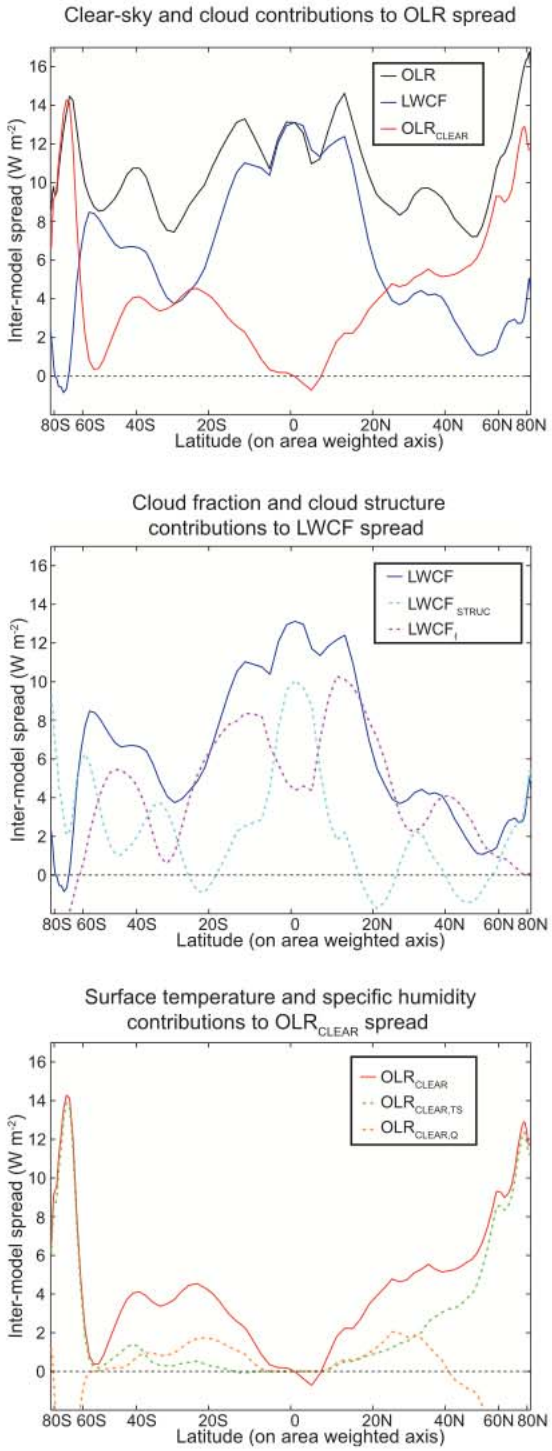

FIG. 7. (a) CMIP3 intermodel spread in OLR decomposed in cloud (LWCF) and clear-sky (OLR_{CLEAR}) components as described in the text. (b) The LWCF contribution to the intermodel spread in OLR decomposed into cloud fraction ($LWCF_f$) and cloud structure ($LWCF_{STRUC}$) components. (c) The OLR_{CLEAR} contribution to the intermodel spread in OLR decomposed into components that are linearly congruent with the surface temperature spread ($OLR_{CLEAR,TS}$) and the negative vertically integrated specific humidity spread ($OLR_{CLEAR,Q}$).

Plugging Eq. (14) into Eq. (15) and rearranging, we find an expression for LWCF in terms of the cloud fraction (f) and cloud OLR properties:

$$\mathrm{LWCF} = f(\mathrm{OLR}_{\mathrm{CLEAR}} - \mathrm{OLR}_{\mathrm{CLOUD}}) \equiv f(C_{\mathrm{STRUC}}). \quad (16)$$

Equation (16) states that LWCF is a consequence of the fraction of the scene that is cloudy and the optical properties of the cloud (C_{STRUC}). For example, two models with the same f could have very different LWCF*s* due to different cloud-top heights (Hartmann et al. 1992). The intermodel spread in LWCF is divided into components due to intermodel differences in f and C_{STRUC} by decomposing f and C_{STRUC} into the ensemble average ($\tilde{}$) and model departures from the ensemble average ($\langle\,\rangle$) at each latitude:

$$\begin{aligned}\mathrm{LWCF} &= (\tilde{f} + \langle f \rangle)(\tilde{C}_{\mathrm{STRUC}} + \langle C_{\mathrm{STRUC}} \rangle) \\ &= \tilde{f}\tilde{C}_{\mathrm{STRUC}} + \tilde{f}\langle C_{\mathrm{STRUC}} \rangle + \langle f \rangle \tilde{C}_{\mathrm{STRUC}} \\ &\quad + \langle f \rangle \langle C_{\mathrm{STRUC}} \rangle. \end{aligned} \quad (17)$$

The first term on the right-hand side does not contribute to the intermodel spread in LWCF. The second and third terms correspond, respectively, to the contributions of cloud structure differences and cloud fraction differences to the intermodel spread in LWCF. The last term is substantially smaller than the other terms at all latitudes (not shown).

Intermodel differences in f are responsible for the majority of the intermodel OLR spread in the subtropics and SH storm-track region and approximately 50% of the intermodel OLR spread in the NH storm-track region (Fig. 7b). Differences in C_{STRUC} are responsible for the vast majority of the intermodel spread of LWCF in the deep tropics. In the polar regions (poleward of 60°), intermodel differences in LWCF are uncorrelated with cloud fraction differences, suggesting that differences in cloud optical properties (as opposed to cloud amount) are responsible for differences in LWCF in this region (Curry and Ebert 1992).

The contribution of $\mathrm{OLR}_{\mathrm{CLEAR}}$ to the OLR spread is subdivided into components that are linearly congruent (Thompson and Solomon 2002) with the intermodel spread in surface temperature and the negative vertically integrated specific humidity as follows. The correlation coefficient between intermodel differences in $\mathrm{OLR}_{\mathrm{CLEAR}}$ and surface temperature (or the negated specific humidity) is multiplied by the $\mathrm{OLR}_{\mathrm{CLEAR}}$ spread at each latitude. The intermodel differences in

surface temperature explain the vast majority of the intermodel spread in OLR_{CLEAR} in the NH extratropics and make the largest contribution to the OLR spread in the polar regions of both hemispheres (Fig. 7c). This spatial structure mimics the intermodel spread in surface temperature spread ($R^2 = 0.95$), which features values of approximately 7 K in the polar regions (2s) and less than 2 K equatorward of 40° (not shown). The regression coefficient between surface temperature and OLR_{CLEAR} for all grid points and models considered together is 2.1 W m^{-2} K^{-1}, which is consistent with other estimates of the linear parameterization of OLR with surface temperature (Warren and Schneider 1979). We understand these results as follows. Per unit perturbation of surface temperature, the OLR changes by approximately 2 W m^{-2} with some regional dependence.[7] Thus, the OLR_{CLEAR} spread scales as the surface temperature spread times approximately 2 W m^{-2} K^{-1} with higher temperatures corresponding to larger OLR values.

We also expect OLR_{CLEAR} to be negatively correlated with the water vapor content of the upper atmosphere due to the greenhouse effect. Indeed, intermodel differences in vertically integrated water vapor explain a portion of the OLR_{CLEAR} spread in the subtropics that was not previously explained by intermodel differences in surface temperature (Fig. 7c), with higher vapor content corresponding to lower OLR values due to the raising of the effective emission level. In the high latitudes the opposite is true; high vapor content corresponds to more OLR due to the positive correlation between upper-tropospheric water vapor and surface temperature (not shown) that is absent in the subtropics. The intermodel differences in high-latitude water vapor content are highly correlated with surface temperature differences and the intermodel differences in water vapor explain a negligible amount of the intermodel spread in OLR_{CLEAR} beyond the spread expected from the water vapor and surface temperature covariance and the relationships between surface temperature and OLR_{CLEAR}: removing the intermodel differences in water vapor that are linearly congruent with the intermodel differences in surface temperature to define the "residual water vapor" content results in a near-zero correlation between intermodel differences in OLR_{CLEAR} and the residual water vapor in the high latitudes (not shown).

In summary, the intermodel spread in OLR is a consequence of nearly equal contributions from clear-sky and cloud processes with the cloud processes playing a dominant role in the lower latitudes and clear-sky processes dominating the extratropics. The cloud contribution is due to differences in both cloud fraction and cloud structure while the clear-sky contribution is primarily due to surface temperature differences with the exception of the subtropics where intermodel differences in water vapor also play a role.

b. *Intermodel spread in* OLR*

The contributions to the OLR spread that were discussed in the previous subsection are projected onto the intermodel spread in OLR* in this section. The spread in OLR* is a consequence of the magnitude of the spread in the component contributions to OLR (previously discussed) and the spatial decorrelation length scale of those processes. For instance, even though the cloud fraction explains a large amount of the OLR spread at each latitude, it would be poorly correlated with the spread in OLR* if the cloud fraction anomalies were local (poorly correlated with anomalies at adjacent latitudes) as opposed to regional or global scales. Sliding one-point correlation maps of the intermodel differences OLR_{CLEAR} and LWCF suggest that intermodel differences in both fields are regional in scale (not shown); individual models tend to have OLR_{CLEAR} and LWCF anomalies that extend over the entire tropical region, storm-track region, or polar regions with no significant correlation between anomalies in one region and the other region. The meridional decorrelation length scale (where the spatial autocorrelation is equal to e^{-1}) of the OLR_{CLEAR} anomalies is of order 15° latitude in the extratropics (≈30° in the tropics) and is slightly longer than that of LWCF.

We define OLR^*_{CLEAR} and OLR^*_{LWCF} for each model by substituting OLR_{CLEAR} and LWCF into the integrand of Eq. (6) with the limits of integration defined from the total OLR field. The intermodel spread in OLR^*_{CLEAR} is 0.52 PW (0.52 PW) and the intermodel spread in OLR^*_{LWCF} is 0.50 PW (0.48 PW) in the NH (SH; see Table 5). The near equality of the clear-sky and cloud contributions to OLR* spread is consistent with the relative contributions of OLR_{CLEAR} and LWCF to the OLR spread at each latitude (Fig. 7) and the fact that both intermodel differences (OLR_{CLEAR} and LWCF) have similar decorrelation length scales. In the NH (SH), 44% (35%) of the intermodel variance in OLR* is due to differences in OLR^*_{CLEAR} and 40% (23%) is due to differences in OLR^*_{LWCF} (Table 5).

We further subdivide OLR^*_{LWCF} into cloud fraction and cloud structure components by use of Eq. (17). Intermodel differences in cloud fraction and cloud structure make nearly equal contributions to the intermodel spread in OLR^*_{LWCF} (Table 5). This result is consistent

[7] The regression of surface temperature onto OLR_{CLEAR} at each latitude shows larger values in the dry subtropics and lower values in the high latitudes.

TABLE 5. (top) Division of OLR* spread into clear-sky (OLR^*_{CLEAR}) and cloud components (OLR^*_{LWCF} – top rows) and (middle) the subsequent division of the cloud contribution into cloud fraction ($OLR^*_{LWCF,f}$) and cloud structure ($OLR^*_{LWCF,STRUC}$) components. (bottom) The correlation of the OLR^*_{CLEAR} spread with the equator-to-pole contrast of surface temperature (TS*) and specific humidity (Q^*).

	NH		SH	
	Spread − 2s	R^2	Spread − 2s	R^2
	Division of OLR* into clear-sky and cloud components; correlations with OLR*			
OLR*	0.58 PW	1.00	0.46 PW	1.00
OLR^*_{CLEAR}	0.52 PW	0.44	0.52 PW	0.35
OLR^*_{LWCF}	0.50 PW	0.40	0.48 PW	0.23
	Division of $\mathbf{OLR^*_{LWCF}}$ into fraction and structure components; correlation with $\mathbf{OLR^*_{LWCF}}$			
$OLR^*_{LWCF,f}$	0.44 PW	0.47	0.50 PW	0.30
$OLR^*_{LWCF,STRUC}$	0.38 PW	0.39	0.52 PW	0.19
	$\mathbf{OLR^*_{CLEAR}}$ correlation with TS* and Q*			
TS*	3.0 K	0.81	1.8 K	0.85
Q^*	2.6 kG m^{-2}	0.12	1.6 kG m^{-2}	0.08

with the previous conclusion that cloud structure and cloud fraction make comparable magnitude contributions to the spread in LWCF with some regional dependence (Fig. 7) and that intermodel differences in cloud fraction and cloud structure are regional in scale (have similar decorrelation length scales; not shown).

The relationship between the equator-to-pole gradient in surface temperature and OLR^*_{CLEAR} is analyzed by defining TS*, the surface temperature anomaly (from the global average) averaged over the extratropics:

$$TS^* = \frac{\int_{x(OLR'=0)}^{1} TS'(x)\,dx}{\int_{x(OLR'=0)}^{1} dx}. \quad (18)$$

Intermodel differences in TS* explain 81% (85%) of the intermodel spread in OLR^*_{CLEAR} (Table 5). The regression coefficient between TS* and OLR^*_{CLEAR} is 0.21 PW K^{-1}, which corresponds to a 2.0 W m^{-2} OLR_{CLEAR} anomaly per unit temperature anomaly averaged over the polar cap; this number is consistent with linear parameterizations of OLR from surface temperature (Warren and Schneider 1979). A similar quantity for the equator-to-pole contrast in specific humidity, Q^*, can be defined by substituting the vertically integrated specific humidity into the integrand of Eq. (18). In neither hemisphere is Q^* significantly correlated with OLR^*_{CLEAR} (Table 5).

In summary the intermodel spread in OLR* is a consequence of nearly equal magnitude contributions from clear-sky and cloud processes. Intermodel differences in both cloud structure and cloud fraction contribute to the spread in OLR^*_{LWCF}, and the vast majority of the OLR^*_{CLEAR} spread is due to intermodel differences in the surface temperature gradient.

c. *Relationship between* OLR* *and* ASR*

We gain further insight into why intermodel differences in OLR* and ASR* do *not* compensate for each other by analyzing the meridional structures of the ASR and OLR anomalies associated with a "typical" ASR* anomaly from the ensemble average. We regress a normalized index of ASR* onto the intermodel spread in zonal average ASR, OLR, LWCF, and OLR_{CLEAR} (Fig. 8). The resulting ASR curve shows the anticipated structure of an ASR* anomaly with anomalously high values in the tropics and low values in the extratropics; both tropical and extratropical anomalies in $\mathbf{a}_{P,ATMOS}$ contribute to a typical ASR* anomaly. In contrast, the OLR anomaly associated with an ASR* anomaly only has appreciable magnitude in the tropics that is due to LWCF anomalies of the same sign as the ASR anomalies. We interpret this result as the compensation between LWCF and shortwave cloud forcing in the tropics (Kiehl 1994; Hartmann et al. 2001): the same cloud properties that increase the reflection of shortwave radiation also reduce OLR by raising the effective longwave emission level (more positive LWCF). This compensation is not complete over the tropics for the intermodel spread (cf. the magnitude of the OLR and ASR curves in the tropics in Fig. 8). Over the extratropics, there is little compensation between ASR and OLR anomalies in a typical ASR* anomaly because (i) the OLR spread is a consequence of both clear-sky and cloud properties in this region whereas the ASR spread is primarily due to cloud properties and (ii) the cloud properties that determine the intermodel spread in $\mathbf{a}_{P,ATMOS}$ are different from the cloud properties

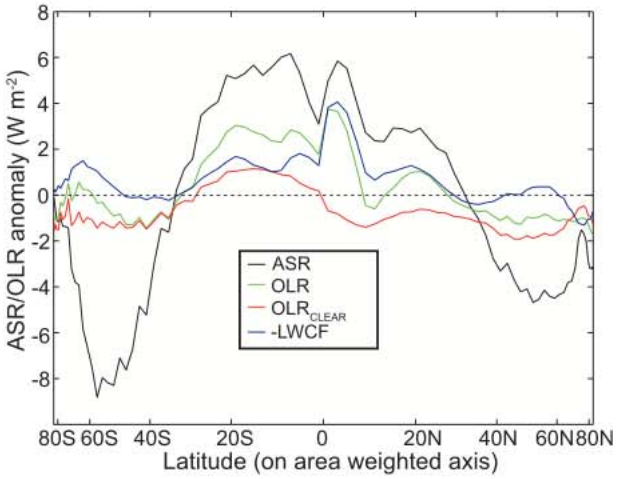

FIG. 8. Regression of the normalized intermodel spread in ASR* on to the intermodel anomalies of ASR (black), OLR (green), OLR_{CLEAR} (red), and LWCF (blue). The resulting curves are the radiative anomalies associated with a one-standard deviation ASR* anomaly.

that determine the OLR spread.[8] As a consequence, ASR and OLR anomalies are poorly correlated with each other over the extratropics leading to ASR* and OLROLR* spread that is only partially compensating.

5. Summary and discussion

The peak meridional heat transport ($MHT_{MAX}MHT_{MAX}$) in the climate system was diagnosed as the difference between the equator-to-pole contrast of ASR (ASR*) and OLR (OLR*). The results show 65% (59%) of the observed ASR* in the NH (SH) is a consequence of the meridional distribution of incident solar radiation at the TOA while the remaining 35% (41%) is due to the meridional distribution of planetary albedo. We have demonstrated that the vast majority (86% and 94% in the NH and SH, respectively) of the meridional gradient of planetary albedo is a consequence of atmospheric as opposed to surface reflection. These results suggest that surface albedo plays a very minor role in setting the equator-to-pole gradient in ASR compared with atmospheric reflection (e.g., cloud distribution).

The total equator-to-pole gradient in absorbed solar radiation, ASR*, and its partitioning into atmospheric and surface albedo components found in the observations is well replicated in the ensemble average of the CMIP3 PI model simulations in the NH. However, in the SH, the ensemble average ASR* is smaller than that observed due to a smaller than observed equator-to-pole contrast in $a_{P,ATMOS}(ASR^*_{ATMOS})$. As a consequence, the ensemble average MHT_{MAX} is 0.6 PW smaller than the observed value in the SH.

The CMIP3 simulations of the PI climate system exhibit a remarkably large spread (of order 1 PW or 20%) in MHT_{MAX} that exceeds the projected change in MHT_{MAX} under global warming (i.e., the change in the $2 \times CO_2$ simulations) by a factor of approximately 5 (Hwang and Frierson 2011). This spread is due to intermodel differences in the equator-to-pole gradient in ASR (ASR*) and is uncorrelated with intermodel differences in the equator-to-pole gradient in OLR (OLR*). The intermodel spread in ASR* results from model differences in the meridional gradient of a_P that are primarily (94%) due to differences in cloud reflection ($a_{P,ATMOS}$). As a consequence, the intermodel differences in maximum meridional heat transport in the climate models is primarily due to differences in the shortwave optical properties of the atmosphere (Fig. 6); intermodel differences in cloud reflection of shortwave radiation explain 84% of the intermodel spread in MHT_{MAX} in the SH and 63% of the spread in NH (Table 4). Our definition of MHT_{MAX} in terms of ASR* and OLR* is a useful tool for analyzing the MHT_{MAX} and its intermodel spread because the meridional contrast of ASR and OLR are governed by different physical processes in the models: ASR* is primarily controlled by cloud reflection whereas cloud fraction, cloud structure, and surface temperature contribute to OLR*.

Our methodology analyzes the total meridional heat transport in both the atmosphere and ocean and does not distinguish between atmospheric and oceanic energy transport. Provided both the atmosphere and ocean are in equilibrium and the ASR is fixed, the local OLR and hence OLR* is a function of the total (atmosphere plus ocean) energy flux convergence, and does not depend on how the energy is transported. Therefore, from the perspective of the TOA radiative budget analyzed in this study, the intermodel spread in MHT_{MAX} is, in principle, equally susceptible to the differences in atmospheric and oceanic heat transport. The intermodel differences in atmospheric and oceanic heat transport are calculated by analyzing the surface and atmospheric energy budgets separately. We find that approximately two-thirds of the intermodel spread in MHT_{MAX} is due to differences in atmospheric heat transport and the remaining one-third is a consequence of differences in oceanic heat

[8] The intermodel spread in $a_{P,ATMOS}$ in the Southern Ocean is poorly correlated with cloud fraction whereas the spatial variations in $a_{P,ATMOS}$ within a given model are well correlated with cloud fraction. This result suggests that intermodel variations in the parameterization of cloud albedo as opposed to cloud fraction differences are responsible for the $a_{P,ATMOS}$ spread.

transport (not shown). We hope to further analyze this result in future work.

Our results indicate that, in the present climate, MHT_{MAX} is mainly determined by the shortwave optical properties of the atmosphere (i.e., cloud distribution) and suggests that MHT_{MAX} is largely insensitive to subtleties in the model dynamics that contribute to the heat transport (Stone 1978). We can understand this result within the context of simplified energy balance models. In the annual mean, the extratropical deficit in ASR, ASR*, is balanced by the sum of OLR anomalies relative to the global mean (OLR*) and meridional heat transport into the extratropics (MHT_{MAX}). If the heat transport is diffusive along the surface temperature gradient and the OLR anomaly is proportional to the surface temperature anomaly from the global mean (as in Budyko 1969; Sellers 1969, among others), then both the extratropical OLR anomaly and MHT_{MAX} are proportional to the same equator-to-pole temperature gradient. The ratio between MHT_{MAX} and OLR* is then dictated by the relative efficiencies of large-scale heat diffusion and radiation to space which is commonly called d in the literature [see Rose and Marshall (2009) for a review]. If two climate models had different d values yet the same ASR*, MHT_{MAX} would differ between the models and the intermodel spread in ASR*, and OLR* would be anticorrelated. For example, a more diffusive model (e.g., a model with more vigorous baroclinic eddies) would have more MHT_{MAX} and less OLR* and vice versa. In contrast, if d were nearly equal among climate models but ASR* varied, then the MHT_{MAX} and OLR* would be proportional to ASR* with a regression coefficient dictated by the relative efficiency of dynamic and radiative heat exports [equal to $d/d + 1$ and $1/d + 1$, respectively; see Donohoe (2011)]. The positive correlation between ASR* and OLR* (Fig. 3c) suggests that the CMIP3 suite of climate models all have similar d values such that MHT_{MAX} is dictated by ASR*, which, in turn, we have demonstrated is controlled by the meridional distribution of the simulated clouds. Furthermore, the relatively steep slope between MHT_{MAX} and ASR* (a regression coefficient of 0.64 in the NH and 0.85 in the SH; see Fig. 3a) as compared to the relatively shallow slope between OLR* and ASR* (a regression coefficient of 0.36 in the NH and 0.15 in SH; see Fig. 3c) suggests that d is greater than unity; the dynamic export of heat out of the tropics (MHT_{MAX}) is a more efficient pathway for achieving local energy balance than is the radiative (OLR) export of energy. We note that Lucarini et al. (2011) also found that, on interannual time scales, the radiative feedback at the equator-to-pole scale is weaker than the meridional heat transport feedback in the CMIP3 models. Thus, per the unit ASR* anomaly due to the model differences in atmospheric reflection, the extratropical energy budget will be balanced primarily by a MHT_{MAX} anomaly and secondarily by an OLR* anomaly.

Our results have implications for understanding the changes in MHT_{MAX} due to global warming. Preliminary analysis of the CMIP3 model experiments where CO_2 is increased 1% yr^{-1} to doubling suggests that reduced sea ice extent causes a decrease in the surface contribution to ASR* and that cloud changes, which differ markedly between models (Bony et al. 2006), cause large intermodel differences in the atmospheric contribution to ASR* that overwhelm the more predictable ASR* change due to sea ice melting. We also expect, and find, a reduction in d in a warmer planet because (a) moist static energy gradients are enhanced relative to temperature gradients in a warmer world due to nonlinearities in the Clasius–Clapereyon equation (Hwang and Frierson 2011), leading to more meridional heat transport for the same surface temperature gradient, and (b) a warmer and moister atmosphere emits longwave radiation from a higher elevation where the meridional temperature gradient is reduced relative to that at the surface, thereby reducing OLR* for the same surface temperature gradient. Therefore, in the limit of an ASR* that is climate-state invariant, we expect that global warming will increase MHT_{MAX} and decrease OLR*. However, the large intermodel differences in the change in ASR* due to cloud changes overwhelm the expectation that MHT_{MAX} increases in a warmer world—so much so that the ensemble average change in MHT_{MAX} from the CMIP models is not statistically different from zero.

Acknowledgments. We acknowledge the modeling groups, the Program for Climate Model Diagnosis and Intercomparison (PCMDI), and the WCRP's Working Group on Coupled Modelling (WGCM) for their roles in making available the WCRP CMIP3 multimodel dataset. Support of this dataset is provided by the Office of Science, U.S. Department of Energy. This work was inspired by conversations with Gerard Roe, Kyle Armour, Ed Blanchard Wrigglesworth IV, Brian Rose, John Marshall, Valerio Lucarini, Rowan Sutton, Jonathan Gregory, and Dargan Frierson. This work was supported by the Tamaki Foundation.

REFERENCES

Bony, S., and Coauthors, 2006: How well do we understand climate change feedback processes? *J. Climate,* **19,** 3445–3482.

Budyko, M., 1969: The effect of solar radiation variations on the climate of the earth. *Tellus,* **21,** 611–619.

Curry, J. A., and E. E. Ebert, 1992: Annual cycle of radiation fluxes over the Arctic Ocean: Sensitivity to cloud optical properties. *J. Climate,* **5,** 1267–1280.

Donohoe, A., 2011: Radiative and dynamic controls of global scale energy fluxes. Ph.D. thesis, University of Washington, 137 pp.

——, and D. Battisti, 2011: Atmospheric and surface contributions to planetary albedo. *J. Climate,* **24,** 4401–4417.

Enderton, D., and J. Marshall, 2009: Controls on the total dynamical heat transport of the atmosphere and oceans. *J. Atmos. Sci.,* **66,** 1593–1611.

Fasullo, J. T., and K. E. Trenberth, 2008a: The annual cycle of the energy budget. Part I: Global mean and land–ocean exchanges. *J. Climate,* **21,** 2297–2312.

——, and ——, 2008b: The annual cycle of the energy budget. Part II: Meridional structures and poleward transports. *J. Climate,* **21,** 2313–2325.

Graves, C., W. Lee, and G. North, 1993: New parameterizations and sensitivities for simple climate models. *J. Geophys. Res.,* **98** (D3), 5025–5036.

Hartmann, D. L., M. E. Ockert-Bell, and M. L. Michelsen, 1992: The effect of cloud type on earth's energy balance: Global analysis. *J. Climate,* **5,** 1281–1304.

——, L. Moy, and Q. Fu, 2001: A global surface albedo model. *J. Climate,* **14,** 4495–4511.

Held, I., and B. Soden, 2006: Robust responses of the hydrological cycle to global warming. *J. Climate,* **19,** 5686–5699.

Hwang, Y., and D. Frierson, 2011: Increasing atmospheric poleward energy transport with global warming. *Geophys. Res. Lett.,* **37,** L24807, doi:10.1029/2010GL045440.

Kiehl, J., 1994: On the observed near cancellation between longwave and shortwave cloud forcing in tropical regions. *J. Climate,* **7,** 559–565.

Lucarini, V., and F. Ragone, 2011: Energetics of climate models: Energy balance and meridional enthalpy transports. *Rev. Geophys.,* **49,** RG1001, doi:10.1029/2009RG000323.

——, K. Fraedrich, and F. Ragone, 2011: New results on the thermodynamical properties of the climate system. *J. Atmos. Sci.,* **68,** 2438–2458.

Meehl, G. A., C. Covey, T. Delworth, M. Latif, B. McAvaney, J. F. B. Mitchell, R. J. Stouffer, and K. E. Taylor, 2007: The WCRP CMIP3 multimodel dataset: A new era in climate change research. *Bull. Amer. Meteor. Soc.,* **88,** 1383–1394.

North, G. R., 1975: Theory of energy-balance climate models. *J. Atmos. Sci.,* **32,** 2033–2043.

Robock, A., 1980: The seasonal cycle of snow cover, sea ice and surface albedo. *Mon. Wea. Rev.,* **108,** 267–285.

Rose, B., and J. Marshall, 2009: Ocean heat transport, sea ice, and multiple climate states: Insights from energy balance models. *J. Atmos. Sci.,* **66,** 2828–2843.

Rutan, D., F. Rose, N. Smith, and T. Charlock, 2001: Validation data set for CERES surface and atmospheric radiation budget (SARB). *GEWEX/WCRP Newsletter,* Vol. 11, No. 1, International GEWEX Project Office, Silver Spring, MD, 11–12.

Sellers, W. D., 1969: A global climatic model based on the energy balance of the earth-atmosphere system. *J. Appl. Meteor.,* **8,** 392–400.

Solomon, S., D. Qin, M. Manning, M. Marquis, K. Averyt, M. M. B. Tignor, H. L. Miller Jr., and Z. Chen, Eds., 2007: *Climate Change 2007: The Physical Science Basis.* Cambridge University Press, 996 pp.

Stone, P., 1978: Constraints on dynamical transports of energy on a spherical planet. *Dyn. Atmos. Oceans,* **2,** 123–139.

Thompson, D., and S. Solomon, 2002: Interpretation of recent Southern Hemisphere climate change. *Science,* **84,** 895–899.

Trenberth, K. E., and J. M. Caron, 2001: Estimates of meridional atmosphere and ocean heat transports. *J. Climate,* **14,** 3433–3443.

——, and J. T. Fasullo, 2010: Simulation of present day and 21st century energy budgets of the southern oceans. *J. Climate,* **23,** 440–454.

Vonder Haar, T., and A. Oort, 1973: New estimate of annual poleward energy transport by Northern Hemisphere oceans. *J. Phys. Oceanogr.,* **3,** 169–172.

Warren, S., and S. Schneider, 1979: Seasonal simulation as a test for uncertainties in the parameterizations of a Budyko–Sellers zonal climate model. *J. Atmos. Sci.,* **36,** 1377–1391.

Wielicki, B., B. Barkstrom, E. Harrison, R. Lee, G. Smith, and J. Cooper, 1996: Clouds and the Earth's Radiant Energy System (CERES): An earth observing system experiment. *Bull. Amer. Meteor. Soc.,* **77,** 853–868.

Wunsch, C., 2005: The total meridional heat flux and its oceanic and atmospheric partition. *J. Climate,* **18,** 4374–4380.